J Eng Math (2007) 57:333–350
DOI 10.1007/s10665-006-9076-8

ORIGINAL PAPER

Eddy currents in a gradient coil, modeled as circular loops of strips

J. M. B. Kroot · S. J. L. van Eijndhoven · A. A. F. van de Ven

Received: 23 May 2005 / Accepted: 11 July 2006 / Published online: 16 January 2007

Abstract As a model for the z-coil of an MRI-scanner a set of circular loops of strips, or rings, placed on one cylinder is chosen. The current in this set of thin conducting rings is driven by an external source current. The source, and all excited fields, are time-harmonic. The frequency is low enough to allow for an electro-quasi-static approach. The rings have a thin rectangular cross-section with a thickness so small that the current can be assumed uniformly distributed in the thickness direction. Due to induction, eddy currents occur resulting in an edge-effect. Higher frequencies cause stronger edge-effects. As a consequence, the resistance of the system increases and its self-inductance decreases. The Maxwell equations imply an integral equation for the current distribution in the rings. The Galerkin method with Legendre polynomials as global basis functions is applied. This method shows fast convergence, so only a very restricted number of basis functions is needed. The general method is worked out for N ($N \geq 1$) rings, and explicit results are presented for $N = 1$, $N = 2$ and $N = 24$. The derived integral equation and the numerical results of the simulations show that sets of circular rings and plane strips describe the same electromagnetic behavior, thus demonstrating that inductance effects are local.

Keywords Eddy currents · Edge-effect · Legendre polynomials · MRI-scanner · Rings

1 Introduction

Magnetic Resonance Imaging (MRI) is a revolutionary imaging technique that plays an prominent role in medical diagnostics. It provides 3D information for several types of tissue in a body without ionizing radiation. For an extensive overview of MRI, see for example [1, 2].

The main magnet of an MRI-scanner generates a strong static magnetic field. Hydrogen nuclei in the body start spinning and align in this field. A gradient coil creates a gradient in the magnetic field, which is needed to select a slice within the body. In the gradient coils, dynamic currents are generated, inducing a dynamic magnetic field. The gradients provoke a body with spinning nuclei at varying frequencies.

J. M. B. Kroot · S. J. L. van Eijndhoven · A. A. F. van de Ven (✉)
Eindhoven University of Technology
P. O. Box 513, 5600 MB
Eindhoven, The Netherlands
e-mail: a.a.f.v.d.ven@tue.nl

Only from the slice with a certain spin frequency, resonance signals are detected. Three different types of gradient coils, x-, y- and z-coil, vary the magnetic field strength around the centre in the corresponding directions.

Since gradient coils must be switched on and off frequently, the self-inductance plays an important role in the design of gradient coils. Only if the self-inductance is small, switching can be done quickly. One of the major problems in the use of switched gradient coils is the interaction of the rapidly changing fields with the conducting structures in the MRI-scanner including the gradient coils themselves. A dynamic magnetic field produced by a gradient coil induces eddy currents in the conducting structures. The eddy currents cause perturbations on the expected gradient field, leading to blurring in the MR picture, so they should be avoided.

This paper is concerned with the mathematical modeling of the current distribution in a gradient z-coil of given configuration. The model of the coil consists of a finite number of parallel rings, which are considered very thin. They have equal radii, may have different widths, and be positioned at different mutual distances. The distribution of the current in one ring is time- and space-dependent. We consider a time-harmonic source with a relatively small frequency in the order of kHz. Although the rings are mutually distinct, subsets of rings can be driven by one and the same source. The total current through such a subset is then prescribed.

The aim of the modeling is the calculation of the electric current distribution in each ring and from that the resistance and self-inductance of the whole system, each of them depending on the applied frequency. An integral equation is derived for the current distribution and the Galerkin method is used to solve this equation. The most important issue is the choice of the basis functions. It turns out that Legendre polynomials as basis functions are an appropriate choice; they provide a simple analytical expression for the inner products in the Galerkin method. In previous research, Ulicevic et al. [3] modeled the edge-effect for sets of infinitely long plane parallel strips. This model forms the basis of the present work. The analytical approach in this paper leads to an integral equation of the second kind for the current distribution. The asymptotic behavior of the integral kernel is logarithmic and, therefore, we use the Galerkin method with Legendre polynomials as the basis functions. Atkinson [4, 5] proposed methods, such as the Nyström method and the collocation method to solve such an integral equation.

A Maxwell pair, the basic concept in the design of a z-coil, consists of two circular loops of wire carrying currents in opposite directions; see Sect. 4.2 in this paper. A straightforward approach to obtain a better gradient field is to introduce more loops or a coil with multiple turns. Romeo and Hoult [6] and Suits and Wilken [7] describe how to determine the optimal positions of the loops and the intensities of the currents. Optimization methods, such as the conjugate gradient method and the simulated annealing method are used for this by Wong and Jesmanowicz [8] and Crozier and Doddrell [9], respectively. Some basic methods for the design of x- and y-coils are described by Frenkiel et al. [10] and Siebold [11]. Another approach is the target field method of Turner [12]. Approaches using stream functions to determine optimal surface structures are reported among others by Peeren [13, 14], and Tomasi [15]. In [13, 14], the optimal structure is related to a minimization of the magnetic energy; in this approach, currents are assumed static. In [15], the current distribution is discretized by use of one-dimensional wires.

In Sect. 2, we derive the integral equation for the current distribution by applying the Maxwell equations to the geometry of thin conducting rings on a cylinder. The behavior of the kernel function in the integral equation is investigated. In Sect. 3, we present the numerical approach for the problem of the rings and the choice of the basis functions. In Sect. 4, the results of the numerical simulations are presented for different configurations. In Sect. 5, we summarize the conclusions that can be drawn from the analytical and numerical models. One of the main results of this research is that in the design of a coil built up of circular rings, for the calculation of the current distribution it is justified, to a relatively high degree of accuracy, to replace the circular rings by a corresponding set of plane parallel strips. This is primarily due to the logarithmic behavior of the kernel of the governing integral equation.

2 Mathematical analysis

2.1 Model definition

The z-coil consists of a long thin strip of copper wound around a cylinder. It has the shape of a set of parallel rings connected by short joints from one ring to the other. The electromagnetic effects of the joints in the copper are negligible due to another strip just below the joints, which carries a current that roughly cancels out possible disturbances. The width of the strip is a few centimeters and its thickness a few millimeters. The distance between two successive loops varies from a few millimeters to a few centimeters. As a model, we consider a finite number, N, of circular loops of strips, which are parallel and have the same central axis; see Fig. 1. The strips carry a time-harmonic current of frequency ω, with current distribution

$$\tilde{\mathbf{J}}(r,\varphi,z,t) = \mathfrak{Re}\{\mathbf{J}(r,\varphi,z)\mathrm{e}^{-\mathrm{i}\omega t}\}. \tag{1}$$

Here, we used cylindrical coordinates (r,φ,z), with the z-axis along the central axis of the cylinder. The radius of the circular loops is R and so they are part of the cylindrical surface S_c

$$S_c = \{(r,\varphi,z) \in \mathbb{R}^3 | r = R, -\pi \leq \varphi \leq \pi, -\infty < z < \infty\}. \tag{2}$$

Each separate strip is of uniform width and all strips have the same thickness h. However, not all the strips have to be of the same width and the mutual distances may be different. A typical measure for the thickness is $h = 2.5 \times 10^{-3}$ m. The cross-section of a strip is a narrow rectangle, meaning that the thickness h is small compared to the width, but more relevant for us is the ratio of h with respect to the penetration depth δ. The penetration depth is characteristic for the distance in thickness direction over which the current density changes essentially. If δ is larger than half the width $h/2$ of the ring, the current density is approximately uniform in thickness direction. In the latter case, we assume that the strips are infinitely thin, and replace the current density $\mathbf{J}$ (in A/m^2) by the current per unit of length $\mathbf{j}$ (in A/m), defined as

$$\mathbf{j} = \int_R^{R+h} \mathbf{J}\,\mathrm{d}r \approx h\mathbf{J}. \tag{3}$$

The penetration depth is defined as $\delta = \sqrt{2/\mu\sigma\omega} = \sqrt{1/\pi\mu\sigma f}$, where $f = \omega/2\pi$; see e.g. [16, Eq. 35.7]. The values for the electric conductivity σ, the magnetic permeability $\mu = \mu_0$ and the electric permittivity $\epsilon = \epsilon_0$ (all the media are non-polarizable and non-magnetizable, and the copper rings are isotropic, homogeneous, linear conductors) are shown in Table 1. For frequencies $f < 10^4$ Hz, we find that $\delta > h/2$, so that the replacement of $\mathbf{J}$ by $\mathbf{j} = h\mathbf{J}$ is justified. From now on, we refer to the circular loops of infinitely thin strips as *rings*.

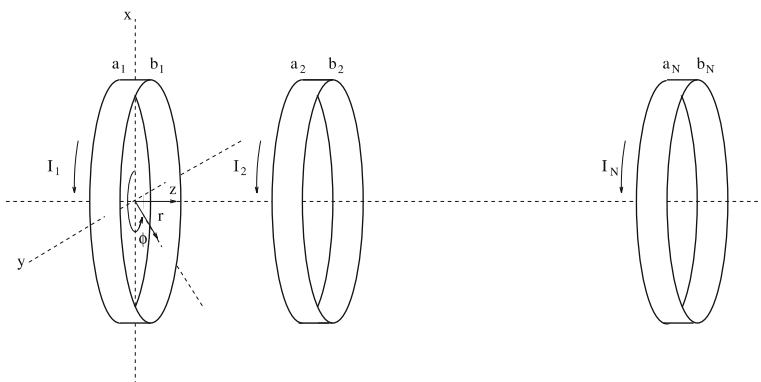

Fig. 1 The geometry of the model, consisting of circular loops of strips

Table 1 Values of geometrical and material constants for copper rings

Symbol	Name	Value
σ	Electric conductivity	$5{\cdot}8 \times 10^{7}\,\Omega^{-1}\,\mathrm{m}^{-1}$
μ	Magnetic permeability	$4\pi \times 10^{-7}\,\mathrm{H\,m}^{-1}$
ϵ	Electric permittivity	$8{\cdot}85 \times 10^{-12}\,\mathrm{C\,m}^{-1}$
h	Thickness of the rings	$2{\cdot}5 \times 10^{-3}\,\mathrm{m}$

The N rings occupy the surface $S_\cup \subset S_c$, described in cylindrical coordinates by

$$S_\cup = \sum_{p=1}^{N} S_p, \quad S_p = \{(r,\varphi,z) \in \mathbb{R}^3 \mid r = R, -\pi \le \varphi \le \pi, a_p \le z \le b_p\}. \tag{4}$$

The total current through a ring is $I_p(t) = \Re\mathfrak{e}\{I_p \mathrm{e}^{-\mathrm{i}\omega t}\}$, for $p = 1,\ldots,N$, where each $I_p \in \mathbb{C}$ is a complex amplitude. By G^-, we define the inner region of the surface S_c, and by G^+ the outer region, both being vacuum.

To obtain the mathematical description of our problem, we start from the Maxwell equations for time-harmonic electromagnetic fields. An electro quasi-static approach is applied ($\epsilon\omega/\sigma \ll 1$), implying that the displacement current (i.e., the term $\partial\mathbf{D}/\partial t$ in Ampère's law) and the instationary term $\partial\rho/\partial t$ in the law of conservation of charge are neglected. The result of the latter neglect is a divergence-free current in the rings, i.e., $\nabla\cdot\mathbf{j} = 0$. We denote by $\mathbf{H}$ the magnetic field strength, and by $\mathbf{E}$ the electric field strength, which due to the axial symmetry of the problem are φ-independent. In this quasi-static approach, the Maxwell equations in G^- and G^+, where $\mathbf{j} = \mathbf{0}$, yield; see e.g. Stratton [17, Chapter 1],

$$\nabla\times\mathbf{E} = \mathrm{i}\omega\mu\mathbf{H}, \quad \nabla\cdot\mathbf{E} = \nabla\times\mathbf{H} = \nabla\cdot\mathbf{H} = 0, \quad \mathbf{x} \in G^- \cup G^+, \tag{5}$$

and in the rings $S_\cup$,

$$\nabla\cdot\mathbf{j} = 0, \quad \mathbf{j} = \mathbf{j}^s + \sigma h\mathbf{E}, \quad \mathbf{x} \in S_\cup, \tag{6}$$

where $\nabla\cdot\mathbf{j}$ is the surface divergence of the surface current $\mathbf{j}$, and $\mathbf{j}^s$ is the (spatial part of the time-harmonic) source current.[1] The second equation of (6) is Ohm's law, generalized for including source currents; see e.g. [18, Eq. 2.1.4], [19, Sect. 2.1].

The Eqs. 5–6 are valid for ordinary points, i.e., for points in whose neighborhood the physical properties of the medium vary continuously. The points on the cylinder S_c that are between the rings, are ordinary points; those on the rings, i.e., on $S_\cup$, are not ordinary. At $r = R$, the field components of $\mathbf{H}$ and $\mathbf{E}$ have jumps across the surface $S_\cup$. Denoting the jump across $S_\cup$ by $[\![\ ]\!]$, we have

$$[\![\mathbf{E}\times\mathbf{n}]\!] = [\![\mathbf{H}\cdot\mathbf{n}]\!] = 0, \quad [\![\mathbf{E}\cdot\mathbf{n}]\!] = Q_s, \quad [\![\mathbf{H}\times\mathbf{n}]\!] = -\mathbf{j}, \quad \mathbf{x} \in S_\cup, \tag{7}$$

where $\mathbf{n} = \mathbf{e}_r$, and Q_s is the surface charge. Finally, we need the condition at infinity $\mathbf{H} \to \mathbf{0}$ for $|\mathbf{x}| \to \infty$.

Since the surface current $\mathbf{j} = j_\varphi\mathbf{e}_\varphi + j_z\mathbf{e}_z$ satisfies $\nabla\cdot\mathbf{j} = \mathrm{d}j_z/\mathrm{d}z = 0$, together with the boundary condition that j_z is zero at the edges of the rings, we have $j_z \equiv 0$. Hence,

$$\mathbf{j} = j_\varphi(z)\mathbf{e}_\varphi. \tag{8}$$

The equations 5 for $\mathbf{E}(r,z)$ and $\mathbf{H}(r,z)$ in terms of their components, yield one system for the components $\{E_\varphi, H_r, H_z\}$ (see (16) further on) and one for the components $\{E_r, E_z, H_\varphi\}$. Only the first system is coupled with the current density via the boundary conditions (7); the second system is uniform. Therefore, $\{E_r, E_z, H_\varphi\}$ is identically equal to zero.

[1] Here, we only assume the existence of a source current; how this source current in a particular situation is applied is not relevant for our aims here.

We denote the field components in G^- as $\{E_\varphi^-, H_r^-, H_z^-\}$ and in G^+ as $\{E_\varphi^+, H_r^+, H_z^+\}$, and then the boundary conditions become

$$H_r^-(R,z) = H_r^+(R,z), \quad E_\varphi^-(R,z) = E_\varphi^+(R,z),$$
$$H_z^-(R,z) - H_z^+(R,z) = j_\varphi(z), \quad \text{for } \mathbf{x} \in S_\cup. \tag{9}$$

The tangential component of the electric field E_φ should not only be continuous across the ring surface, but also be continuous with regard to the internal electric field inside the ring, which is governed by Ohm's law. With use of $(6)_2$, this results in the following relation between the electric field at $S_\cup$ and the current in the ring

$$\sigma h E_\varphi^-(R,z) = \sigma h E_\varphi^+(R,z) = j_\varphi(z) - j_\varphi^s(z), \quad z \in S_\cup. \tag{10}$$

To create a current in the rings, we have introduced a primary or source current $\mathbf{j}^s$ in (6). Here, we take the source current uniform on each of the rings. Moreover, we assume that the rings are coupled in groups, and that each group is connected to one and the same source. So, for L different groups S_l, we have L constants $C_l, l = 1, \ldots, L$, with $j_\varphi^s(z) = C_l$ for each group S_l. These constants are related to the prescribed total current in each group as we will show now. For this, we express $j_\varphi^s(z)$ in characteristic functions $\psi_l(z)$, which are zero everywhere except on the rings of group S_l, where they have the value one. The source current $j_\varphi^s(z)$ satisfies

$$j_\varphi^s(z) = \sum_{l=1}^{L} C_l \psi_l(z), \quad z \in S_\cup = \bigcup_{l=1}^{L} S_l. \tag{11}$$

To obtain a well-defined problem description, we need L extra relations, in order to determine the constants $C_1, \ldots, C_L$. For this, we require that the total current in each group of rings is prescribed, according to

$$\int_{-\infty}^{\infty} j_\varphi(z)\psi_l(z)\mathrm{d}z = I_l, \quad l = 1, \ldots, L. \tag{12}$$

In order to make our formulation dimensionless, we scale all length parameters with respect to R and introduce a characteristic current as the average current over all the rings,

$$j^c = \frac{1}{D} \sum_{l=1}^{L} I_l, \tag{13}$$

where $D = \sum_{p=1}^{N} D_p$, the sum of the widths of all rings. We scale the surface current and the magnetic field with respect to j^c and the electric field with respect to $\mathrm{i}\mu\omega R j^c$. These scalings do not really change the formulations presented above. Besides that we have to replace in (12) I_l by $\hat{I}_l = I_l/j^c R$, the only change is in (10), which becomes, with use of (11),

$$\mathrm{i}\kappa E_\varphi^-(1,z) = \mathrm{i}\kappa E_\varphi^+(1,z) = j_\varphi(z) - \sum_{l=1}^{L} C_l \psi_l(z), \tag{14}$$

where

$$\kappa = h\sigma\mu\omega R. \tag{15}$$

2.2 Derivation of the integral formula for the current distribution

First we write out the relevant Maxwell equations of (5) in their components as

$$\frac{\partial E_\varphi}{\partial z} = -H_r, \quad \frac{1}{r}\frac{\partial}{\partial r}(rE_\varphi) = H_z,$$

$$\frac{\partial H_r}{\partial z} - \frac{\partial H_z}{\partial r} = 0, \quad \frac{1}{r}\frac{\partial}{\partial r}(rH_r) + \frac{\partial H_z}{\partial z} = 0. \tag{16}$$

Combining these equations in order to eliminate H_r and H_z, we obtain for the electric field

$$\frac{\partial^2 E_\varphi}{\partial z^2} + \frac{1}{r}\frac{\partial}{\partial r}\left(r\frac{\partial E_\varphi}{\partial r}\right) - \frac{1}{r^2}E_\varphi = 0. \tag{17}$$

This equation is valid for both the inner region G^- and the outer region G^+. We solve (17) by applying a Fourier transform with respect to the variable z, yielding

$$-p^2\hat{E}_\varphi + \frac{1}{r}\frac{\partial}{\partial r}\left(r\frac{\partial \hat{E}_\varphi}{\partial r}\right) - \frac{1}{r^2}\hat{E}_\varphi = 0, \tag{18}$$

where $\hat{E}_\varphi(r,p)$ denotes the Fourier transform of $E_\varphi(r,z)$ with respect to z.
The general solution of (18) is

$$\hat{E}_\varphi^-(r,p) = a(p)I_1(|p|r), \quad 0 \le r < 1, \qquad \hat{E}_\varphi^+(r,p) = b(p)K_1(|p|r), \quad r > 1, \tag{19}$$

where I_1 and K_1 are the modified Bessel functions of order one of the first and second kind, respectively. The coefficients $a(p)$ and $b(p)$ can be found from the boundary conditions (9), transformed to the Fourier domain. For this, we first determine H_r and H_z from (16). Using the Wronskian $W(K_0, I_0) = I_0(|p|)K_1(|p|) + I_1(|p|)K_0(|p|) = 1/|p|$; see [20, Eq. 9.6.15], we obtain

$$\hat{E}_\varphi^-(r,p) = I_1(|p|r)K_1(|p|)\hat{\mathrm{J}}_\varphi(p), \qquad \hat{E}_\varphi^+(r,p) = K_1(|p|r)I_1(|p|)\hat{\mathrm{J}}_\varphi(p), \tag{20}$$

where $\hat{\mathrm{J}}_\varphi(p)$ is the Fourier transform of $j_\varphi(z)$.

For the inverse Fourier transform, we use the convolution principle to obtain

$$E_\varphi^-(r,z) = \int_{-\infty}^{\infty} j_\varphi(\zeta)\mathcal{K}_1(r, z-\zeta)\mathrm{d}\zeta, \quad E_\varphi^+(r,z) = \int_{-\infty}^{\infty} j_\varphi(\zeta)\mathcal{K}_2(r, z-\zeta)\mathrm{d}\zeta, \tag{21}$$

where

$$\mathcal{K}_1(r,z) = \frac{1}{\pi}\int_0^\infty I_1(pr)K_1(p)\cos pz\,\mathrm{d}p, \quad 0 \le r < 1, \tag{22}$$

and

$$\mathcal{K}_2(r,z) = \frac{1}{\pi}\int_0^\infty K_1(pr)I_1(p)\cos pz\,\mathrm{d}p, \quad r > 1. \tag{23}$$

Only on the rings the current is unequal to zero, so that the integrals in (21) have contributions over the surface $S_\cup$ only.

Finally, we substitute the solution for the vector potential on $r = 1$ in (14) to arrive at the integral equation for $j_\varphi(z)$ we are looking for

$$j_\varphi(z) - \mathrm{i}\kappa\int_{S_\cup} j_\varphi(\zeta)\mathcal{K}(z-\zeta)\mathrm{d}\zeta = \sum_{l=1}^{L} C_l\psi_l(z), \quad z \in S_\cup, \tag{24}$$

where

$$\mathcal{K}(z) = \frac{1}{\pi}\int_0^\infty I_1(p)K_1(p)\cos pz\,\mathrm{d}p = \frac{1}{2\pi}Q_{\frac{1}{2}}\left(1 + \frac{1}{2}z^2\right), \tag{25}$$

according to [21, Eq. 6.672.4], where $Q_{\frac{1}{2}}$ is the Legendre function of the second kind of order 1/2; cf. [20, Eq. 8.13.7].

We determine the coefficients C_l in the following way. Let $j_\varphi^{(l)}$ be the solution to (24)–(25) with $C_n = 0$, $n = 1,2,\ldots,L$, $n \ne l$, and $C_l = 1$. Determine the functions $j_\varphi^{(l)}$ for $l = 1,2,\ldots,L$. Then,

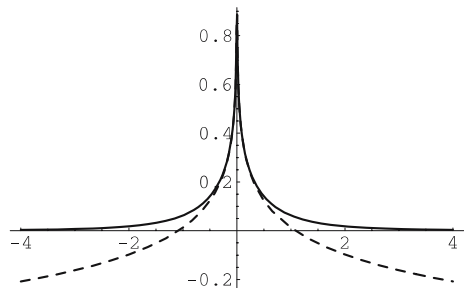

Fig. 2 The kernel $\mathcal{K}(z)$ (solid line) and the approximate function (dashed line)

$j_\varphi(z) = \sum_{l=1}^{L} C_l j_\varphi^{(l)}(z)$. Inserting this expression into (12) with I_l replaced by $\hat{I}_l$, we obtain L linear equations for the L constants C_l in terms of $\hat{I}_l$, from which the C_l's can be solved.

Investigation of the behavior of the kernel function $Q_{\frac{1}{2}}(1+\frac{1}{2}z^2)$ reveals that it has a singularity in $z = 0$. From a numerical point of view, it is important to find an approximate formula that is valid for small z. The asymptotic expansion of $\mathcal{K}(z)$ for $z \to 0$ up to terms of $\mathcal{O}(z^2)$ is

$$\mathcal{K}(z) = -\frac{1}{2\pi}\left(\log|z| - \log 2 + \Psi^{(0)}\left(\frac{3}{2}\right) + \gamma\right) + \mathcal{O}(z^2), \tag{26}$$

where $\Psi^{(0)}(3/2) \approx 0.03649$ ($\Psi^{(0)}$ is the polygamma function; see [20, Eq. 6.4.4]), and $\gamma \approx 0.57722$ (Euler's constant; see [20, Eq. 6.1.3]). In Fig. 2 both the kernel function (solid line) and the series expansion (dashed line) are drawn for $z \in [-4, 4]$. The difference between $\mathcal{K}(z)$ and the series expansion is a regular function, which is exactly equal to zero in $z = 0$ (both its value and its first derivative). In the numerical computations we make use of the approximation for $\mathcal{K}(z)$ given in (26), by splitting up $\mathcal{K}(z)$ in its singular logarithmic part $\mathcal{K}_s(z)$ and its remaining regular part $\mathcal{K}_r(z)$ according to

$$\mathcal{K}(z) = \mathcal{K}_s(z) + \mathcal{K}_r(z), \tag{27}$$

where

$$\mathcal{K}_s(z) = -\frac{1}{2\pi}\left(\log|z| - \log 2 + \Psi^{(0)}\left(\frac{3}{2}\right) + \gamma\right), \tag{28}$$

and $\mathcal{K}_r(z) = \mathcal{K}(z) - \mathcal{K}_s(z)$.

As will be shown in Sect. 4, it is very profitable to use this split-up in the computation of the integral term appearing in the integral equation (24). We can then calculate the singular part analytically and the regular part straightforwardly by numerical means. Thus, we can avoid the time-consuming numerical computation of a logarithmic singular integral.

That the kernel function can be split up into a logarithmic part and a regular part indicates the equivalence between a set of parallel rings and a set of infinitely long parallel strips in one plane. For the strips in one plane, the integral formulation is derived in [3] and it contains a purely logarithmic kernel. Therefore, according to (26), the solution of the ring problem is partly accounted for by the solution of the plane-strip problem. The remaining part of the solution is determined from the regular part of the kernel, in this case, the difference between $\mathcal{K}(z)$ and the $\log|z|$ term.

3 Choice of the basis functions

We have to solve Eq. 24, which we write here as

$$j_\varphi - \mathrm{i}\kappa \mathsf{K} j_\varphi = \sum_{l=1}^{L} C_l \psi_l \tag{29}$$

with

$$(\mathsf{K}f)(z) = \int_{S_\cup} f(\zeta)\mathcal{K}(z-\zeta)\mathrm{d}\zeta. \tag{30}$$

Following [3, Sect. 4], we introduce the orthogonal projection $\mathcal{P}$ on the linear span of the functions ψ_l,

$$(\mathcal{P}f) = \sum_{l=1}^{L} \frac{R}{D_l}(f,\psi_l)\psi_l, \tag{31}$$

where D_l is the sum of the widths of all rings in group S_l. Then,

$$\mathcal{P}j_\varphi = \sum_{l=1}^{L} \frac{R}{D_l}\,\hat{I}_l\psi_l, \tag{32}$$

and

$$(\mathcal{I}-\mathcal{P})j_\varphi - \mathrm{i}\kappa(\mathcal{I}-\mathcal{P})\mathsf{K}(\mathcal{I}-\mathcal{P})j_\varphi = \mathrm{i}\kappa(\mathcal{I}-\mathcal{P})\mathsf{K}\mathcal{P}j_\varphi. \tag{33}$$

Introduce $j_\perp = (\mathcal{I}-\mathcal{P})j_\varphi$ and approximate

$$j_\perp(z) \doteq \sum_{m=1}^{M} \alpha_m\phi_m(z), \quad \phi_m \in \mathrm{ran}(\mathcal{I}-\mathcal{P}). \tag{34}$$

Then,

$$\sum_{m=1}^{M} \alpha_m\phi_m - \mathrm{i}\kappa \sum_{m=1}^{M} \alpha_m(\mathcal{I}-\mathcal{P})\mathsf{K}\phi_m = \mathrm{i}\kappa(\mathcal{I}-\mathcal{P})\mathsf{K}\mathcal{P}j_\varphi, \tag{35}$$

and so for all $n \in \mathbb{N}$,

$$\sum_{m=1}^{M} \alpha_m(\phi_m,\phi_n) - \mathrm{i}\kappa \sum_{m=1}^{M} \alpha_m(\mathsf{K}\phi_m,\phi_n) = \mathrm{i}\kappa(\mathsf{K}\mathcal{P}j_\varphi,\phi_n) = \mathrm{i}\kappa \sum_{l=1}^{L} \frac{R}{D_l}\,\hat{I}_l(\mathsf{K}\psi_l,\phi_n). \tag{36}$$

For the basis functions $\phi_m(z)$ we choose Legendre polynomials P_s, because the kernel of the integral has a logarithmic singularity. If we only consider the logarithmic part of the operator, then a closed-form analytical expression for the integral of the logarithmic function in combination with Legendre polynomials can be found. The analytical solution is shown in (44), further down. Moreover, we expect a current distribution reaching its greatest values along the edges of a ring, and a similar behavior is shown by Legendre polynomials.

We introduce shifted and scaled Legendre polynomials $P_s(z;c,d)$ for the interval $[a,b]$ by

$$P_s(z;c,d) = P_s\Big(\frac{z-c}{d}\Big), \quad z \in [a,b], \tag{37}$$

where

$$c = \frac{b+a}{2}, \quad d = \frac{b-a}{2}. \tag{38}$$

For the current distribution $j_\perp(z)$, the pertinent intervals are $[z_0^{(q)}, z_1^{(q)}]$, $q = 1,\ldots,N$, instead of $[a,b]$. To construct the basis functions, we use a series of shifted and scaled Legendre polynomials, for s running from 0 to S. The Legendre polynomial of degree zero is a constant function of value one. The total current $j_\varphi(z)$ is approximated for a part by L constant functions $\psi_l(z)$. So, for $j_\perp(z)$, $N-L$ constant functions are left, which can differentiate the current distributions in the rings within each group. For these, we choose a set of basis functions $\phi_{0,q}(z)$, where each $\phi_{0,q}(z)$, $q = 1,2,\ldots,N-L$, is a linear combination of characteristic

functions that are either 1 or 0 on a ring. These $N - L$ functions must be chosen in such a way that they are mutually orthogonal and orthogonal to all ψ_l, $l = 1, 2, \ldots, L$. For $1 \le s \le S$ we define

$$\phi_{s,q} = P_s(z; c_q, d_q), \quad q = 1, \ldots, N. \tag{39}$$

In this way, we split up the series expansion (34) into two parts according to

$$j_\perp(z) = \sum_{m=1}^{M} \alpha_m \phi_m(z) = \sum_{s=1}^{S} \sum_{q=1}^{N} \alpha_{s,q} \phi_{s,q}(z) + \sum_{q=1}^{N-L} \alpha_{0,q} \phi_{0,q}(z). \tag{40}$$

We note that the total number of basis functions in (40) is $M = (S + 1)N - L$. Moreover, the requirement that the basis functions are mutually orthogonal, as well as orthogonal, to the functions $\psi_l(z)$, is satisfied by this expansion.

For convenience of notation, we write (36) in a matrix formulation as

$$(\mathbf{G} - \mathrm{i}\kappa \mathbf{A})\mathbf{a} = \mathrm{i}\kappa \mathbf{B}\mathbf{f}. \tag{41}$$

Then,

$$\begin{aligned}
A(s, q; s', q') &= (\mathsf{K}\phi_{s,q}, \phi_{s',q'}) = d_q d_{q'} \int_{-1}^{1} \int_{-1}^{1} P_{s'}(z) P_s(\zeta) \mathcal{K}(d_{q'} z - d_q \zeta + c_{q'} - c_q) \mathrm{d}\zeta \, \mathrm{d}z, \\
G(s, q; s', q') &= (\phi_{s,q}, \phi_{s',q'}) = \frac{2 d_q}{2s + 1} \delta_{ss'} \delta_{qq'}, \\
a(s', q') &= \alpha_{s',q'}, \\
B(s, q; l) &= (\mathsf{K}\psi_l, \phi_{s,q}) = \sum_{q' \in S_l} d_{q'} d_q \int_{-1}^{1} \int_{-1}^{1} P_s(z) \mathcal{K}(d_q z - d_{q'} \zeta + c_q - c_{q'}) \mathrm{d}\zeta \, \mathrm{d}z, \\
f(l) &= \frac{R}{D_l} \hat{I}_l,
\end{aligned} \tag{42}$$

where S_l is the set of all rings of group l.

The integrals in (42), defining the elements of the matrices $\mathbf{A}$ and $\mathbf{B}$, contain a logarithmic singularity if $q = q'$. Therefore, as in (27), we split the integrand into a logarithmic part and a regular part. The regular part can be integrated numerically in a straightforward way. For the integral with the logarithmic part, multiplied by the Legendre polynomials, an analytical expression exists; see [3, Eq. 89] or [22, Eq. 3.61]. Defining

$$\Pi_{ss'} = \frac{d_q^2}{2\pi} \int_{-1}^{1} \int_{-1}^{1} P_s(z) P_{s'}(z) \left[\log(d_q |z - \zeta|) - \log 2 + \Psi^{(0)}\left(\frac{3}{2}\right) + \gamma \right] \mathrm{d}\zeta \, \mathrm{d}z, \tag{43}$$

we obtain

$$\Pi_{ss'} = \begin{cases} \dfrac{8 d_q^2}{2\pi (s + s')(s + s' + 2)[(s - s')^2 - 1]}, & \text{if } s + s' > 0 \text{ even}, \\ 0, & \text{if } s + s' \text{ odd}, \\ \dfrac{d_q^2}{2\pi} \left(4 \log d_q - 6 + 4\Psi^{(0)}\left(\dfrac{3}{2}\right) + 4\gamma \right), & \text{if } s = s' = 0. \end{cases} \tag{44}$$

For different strips, i.e., for $q \neq q'$, no singularities occur.

4 Numerical results

4.1 One ring

We first consider one ring of width $D = 4\,\mathrm{cm}$, centered at $z = 0$. The thickness $h = 2.5\,\mathrm{mm}$, the radius $R = 35\,\mathrm{cm}$ and the amplitude of the total current through the ring $I = 600\,\mathrm{A}$. These values are typical values for a gradient coil.

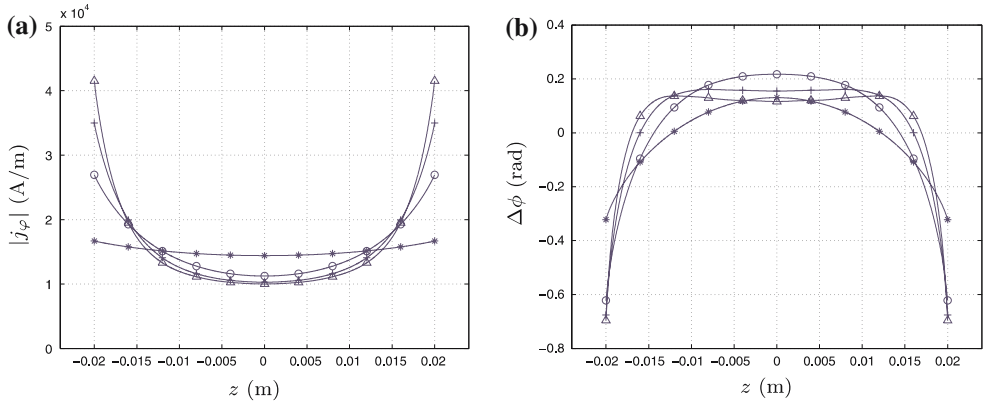

Fig. 3 One ring of 4 cm width with a total current of 600 A at frequencies $f = 100\,\text{Hz}$ (∗), $f = 400\,\text{Hz}$ (○), $f = 700\,\text{Hz}$ (+), $f = 1000\,\text{Hz}$ (△). (**a**) Amplitude of the current distribution; (**b**) Phase-lag with respect to the source current

Figure 3(a) shows the amplitude of the current distribution in the ring for the four frequencies $f = 100,\ 400,\ 700,\ 1,000\,\text{Hz}$. We observe that at the edges the current is higher than in the centre. This *edge-effect*, which is due to the self-inductance of the ring, becomes stronger as the frequency increases. For low frequencies, the current is distributed almost uniformly, whereas for high frequencies the current is more concentrated at the edges. For all frequencies, the average current $j^c = I/D$ is equal to 1.5×10^4 A/m. In [3, Fig. 2], we see a corresponding behavior: The distribution for the current over a ring is in a first-order approximation equal to that of a corresponding plane strip. For practical purposes, i.e., in the design of gradient coils, this first-order approximation is often sufficient. This also holds for sets of two or more rings.

To obtain the time-dependent result for the currents, consider $\mathfrak{Re}\left(\mathbf{J}(z)\mathrm{e}^{-\mathrm{i}\omega t}\right)$. Simulating this case, we observe a phase difference in the system. In Fig. 3(b), the phase-lag $\Delta\phi$ with respect to the source current is shown as function of the position for the four chosen frequencies. The phase difference varies with the frequency. For each frequency only two points are in phase with the source (i.e., $\Delta\phi = 0$). Near the edges the currents are ahead in phase (i.e., negative phase-lag), whereas currents at the center are behind in phase.

The resistance $\bar{R}$ is defined as the time-averaged dissipated power, $\bar{P}_{\text{diss}}$, divided by the squared effective current, I_e^2,

$$\bar{R} = \frac{\bar{P}_{\text{diss}}}{I_e^2} = \frac{1}{\sigma |I|^2} \int_{\mathcal{V}} \mathbf{J} \cdot \mathbf{J}^* \mathrm{d}v. \tag{45}$$

Here, $\mathcal{V}$ denotes the dimensional volume of the ring and the asterisk stands for the complex conjugate. We have computed $\bar{R}$ for different frequencies in the range $[0, 10, 000]$ Hz; see Fig. 4(a). We observe that $\bar{R}$ increases with the frequency, but we also see a decay in the slope of the resistance. The physical interpretation of the first effect is that due to the stronger edge-effects the current flows through a narrower part of the ring, leading to a higher resistance. A decay in the slope of the resistance was also found by Smythe [23, pp. 368–371], for a conducting half-space with a harmonic source current along the surface. The resistance $\bar{R}_{\text{DC}}$ for the static case is verified analytically by taking the circumferential length divided by the conductivity times the cross-sectional surface, i.e.,

$$\bar{R}_{\text{DC}} = \frac{2\pi R}{hD\sigma} \approx 3.74 \times 10^{-4}\,\Omega. \tag{46}$$

In Fig. 4(b), the resistance is shown for frequencies lower than $f = 400\,\text{Hz}$. We observe that the slope of $\bar{R}$ changes, with a point of inflection at $f = f_{\text{char}}$ close to 170 Hz. Such a point of inflection is also observed in the simulations for rings of other widths and for sets of two or more rings. We discuss this phenomenon at the end of this section.

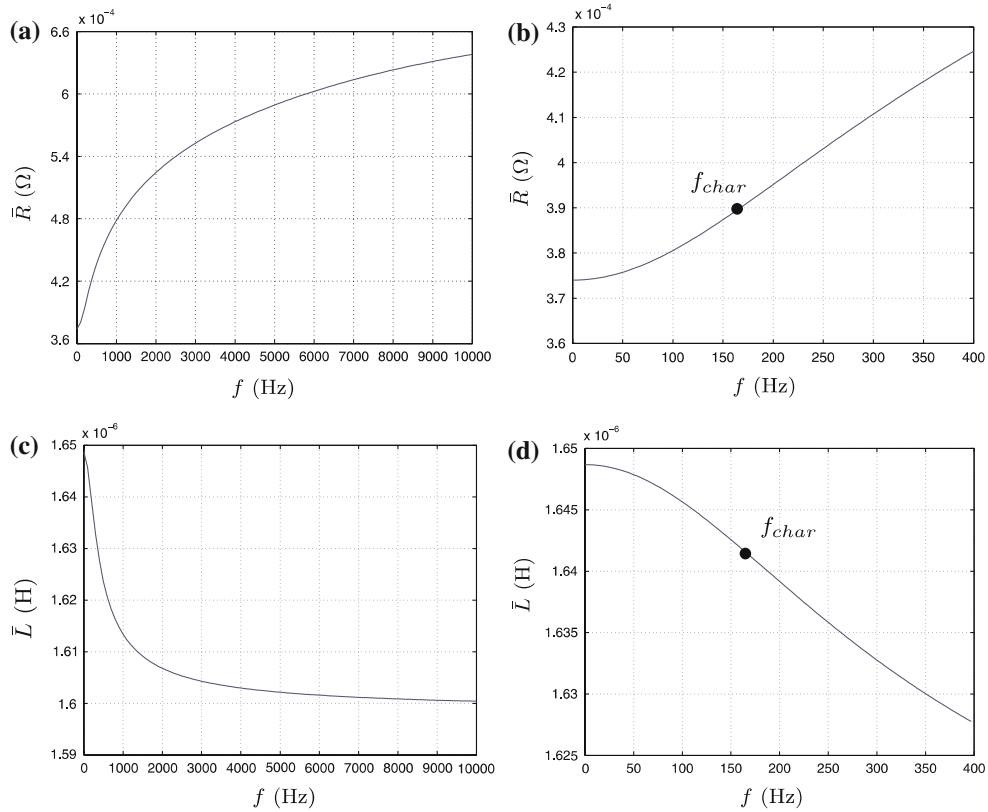

Fig. 4 One ring of 4 cm width with a total current of 600 A. (**a**) Resistance $\bar{R}$ at frequencies up to $f = 10,000$ Hz; (**b**) Resistance $\bar{R}$ at frequencies up to $f = 400$ Hz; (**c**) Self-inductance $\bar{L}$ at frequencies up to $f = 10,000$ Hz; (**d**) Self-inductance $\bar{L}$ at frequencies up to $f = 400$ Hz

The self-inductance $\bar{L}$ is defined as the time-averaged magnetic energy, $\bar{U}_m$, divided by half the squared effective current,

$$\bar{L} = \frac{\bar{U}_m}{\frac{1}{2}I_e^2} = \frac{1}{|I|^2}\int_{\mathcal{V}} \mathbf{A}\cdot\mathbf{J}^* \mathrm{d}v. \tag{47}$$

In Fig. 4(c), the self-inductance $\bar{L}$ is shown for frequencies up to 10,000 Hz. We see that $\bar{L}$ decreases with the frequency. Thus, if the current is jostled near the edges of the ring, as happens in the case of higher frequencies, then the inductive effects decrease.

In the low-frequency range up to 400 Hz, also the self-inductance $\bar{L}$ changes its slope as frequencies increase; see Fig. 4(d). The inflection is at the same characteristic frequency f_{char} as for the resistance.

To investigate the influence of the width of the ring, we have also performed simulations for other values of D. The results look rather similar; the only noticeable effect is that the wider the ring is, the more the current is concentrated near the edges; see [22, Fig. 4.7].

The integral operator K is compact and Hermitian and thus has the following representation:

$$\mathsf{K}f = \sum_{n=0}^{N} \lambda_n(f, u_n)u_n, \tag{48}$$

where $\{\lambda_n\}$ are its eigenvalues and $\{u_n\}$ its orthonormal basis of eigenfunctions. Hence, the solution of (24) satisfies

$$j_\varphi = \sum_{n=0}^{\infty} \left[\frac{1}{1+(\kappa\lambda_n)^2} + \mathrm{i}\, \frac{\kappa\lambda_n}{1+(\kappa\lambda_n)^2} \right] (j_\varphi^s, u_n) u_n, \tag{49}$$

where $1/[1+(\kappa\lambda_n)^2]$ represents the resistive effects, and $\kappa\lambda_n/[1+(\kappa\lambda_n)^2]$ the inductive effects. A characteristic parameter of the system is $\hat{\kappa} = \lambda_0\kappa$. For $\hat{\kappa} < 1$ resistive effects are dominant and for $\hat{\kappa} > 1$ inductive effects.

We can approximate the eigenvalues of the operator K by using the matrix $\mathbf{A}$ from (41). This means that we have to compute the eigenvalues of $\mathbf{G}^{-1}\mathbf{A}$. According to (26), the kernel is well approximated by the logarithmic function, multiplied by a factor $-1/(2\pi)$. Furthermore, due to scaling of the distances on radius R, the integral operator K is related to the integration interval $[-D/(2R), D/(2R)]$. Therefore, we scale the eigenvalues λ_n, $n = 0, 1, 2, \ldots$, of K with the factor $D/(2R)$. Figure 5(a, b) show that the eigenvalues are constrained by

$$\frac{1}{8} \le \frac{2R}{D}\lambda_0 \le \frac{1}{2}\log 2, \qquad \frac{1}{8(n+1)} \le \frac{2R}{D}\lambda_n \le \frac{1}{2n}, \quad n \ge 1. \tag{50}$$

Here, the upper and lower bounds are the same as in the case of an infinitely long plane rectangular strip; see [3]. Moreover, these results are in agreement with those presented by Reade [24].

The dominant eigenvalue $\lambda_0^{(N)}$ is equal to

$$\lambda_0^{(N)} = 0.257\frac{D}{2R}. \tag{51}$$

The characteristic parameter of the system is

$$\hat{\kappa} = 0.257\,\frac{h\sigma\mu\omega D}{2} = 0.807 h\sigma\mu f D. \tag{52}$$

From (52), we see that on curves $fD =$ constant the value of $\hat{\kappa}$ is the same. This means that for a ring of 30 cm width instead of one that is 7.5 times narrower (4 cm), the frequency should be 7.5 times less than in the 4 cm case in order to find the same current distribution. This statement is confirmed by numerical simulations presented in [22, Fig. 4.7. (c)].

Next, we define the characteristic frequency

$$f_{\mathrm{char}} = \frac{1}{0.807\, h\sigma\mu D} = \frac{1.234}{h\sigma\mu D}, \tag{53}$$

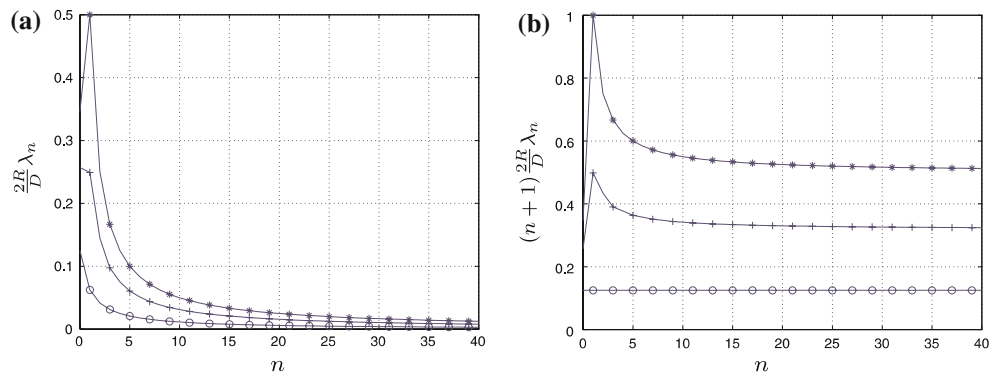

Fig. 5 **(a)** The first 40 scaled eigenvalues of the operator K, $2R\lambda_n/D(+)$, compared with a lower bound $1/(8(n+1))$ $(\circ)$, for $n \ge 0$, and an upper bound $1/(2n)$ $(*)$, for $n \ge 1$ and $\log(2)/2$ for $n = 0$; **(b)** All values multiplied by $n+1$

such that

$$\hat{\kappa} f_{\text{char}} = f. \tag{54}$$

Then, $f = f_{\text{char}}$ represents the frequency at which prevailing resistive effects with respect to inductive effects change into prevailing inductive effects. Presence of the characteristic frequency can well be observed in the graphs of the resistance and the self-inductance against the frequency. Note that for a 4 cm ring the characteristic frequency is $f_{\text{char}} = 167.0$ Hz, according to (53).

4.2 The Maxwell pair

The second example we consider, is a special configuration of two rings. With a pair of rings we are able to create a gradient in the axial component of the magnetic field. The principle of a gradient coil is based on the properties of a Maxwell pair. A Maxwell pair consists of two circular loops of wires of equal radii, placed coaxial and parallel. We use cylindrical coordinates with the z-axis the central axis of the wire loops. If both wires are at equal distance from the origin and carry a current in anti-phase, then the B_z-field has a gradient in the origin. It has been proved that for a mutual distance between the wires equal to $R\sqrt{3}$, the field has no second, third and fourth order z-dependence; see [25, Sect. 2.4]. In other words, at this distance the optimal linear field is achieved.

In the design of gradient coils, one uses a stream function approach, which results in a pattern of streamlines; see e.g., [13–15]. For the manufacture of the coils, copper strips are placed on this pattern. For low frequencies and narrow strips, the currents cause a magnetic field that approximates the design field. However, increasing the frequencies or increasing the widths of the strips causes errors, which lead to unacceptable deviations in the gradient of the magnetic field.

In this section we consider a pair of rings of 4 cm width and a pair of rings of 30 cm width. For a uniform distribution of the current in the rings (comparable with the DC situation) the distance between the rings for an optimal linearity of the B_z-field is equal to 60.8 cm for the 4 cm case and 71.4 cm for the 30 cm case. In order to obtain a desired gradient of $1.0 \times 10^4 \mu$T/m, the current in the 4 cm rings must be 1526.0 A and in the 30 cm rings 1841.6 A. In Fig. 6(a, b), the amplitudes of the current distributions and the z-component of the magnetic field at the z-axis are shown for $f = 1,000$ Hz, for both cases. The gradient of the field is only approximately equal to 1.0×10^4 μT/m here, but there is no visible difference on the scale of this figure. In Fig. 7 we zoom in on the differences between the B_z-field at the z-axis at $f = 0$ Hz and at $f = 100, 400, 700, 1,000$ Hz, for the 4(a) and 30(b) cm case. We observe that the deviation from the ideal value of 1.0×10^4 μT/m increases with the frequency. For a frequency of 1,000 Hz the error in the

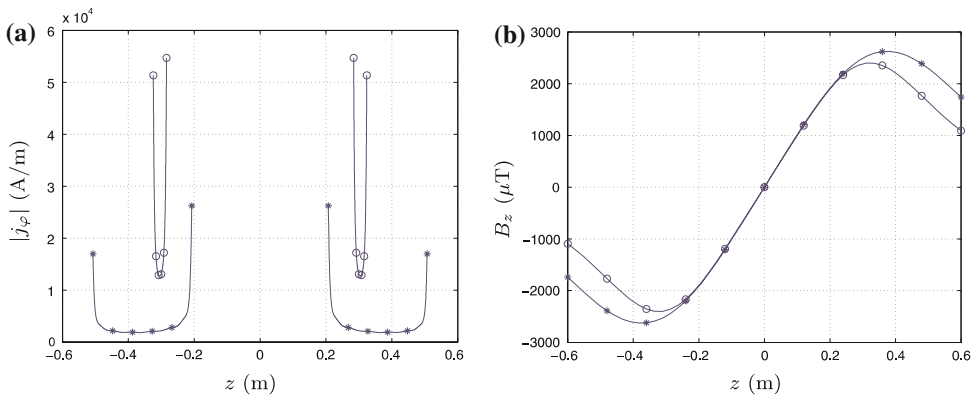

Fig. 6 Two rings of 4 cm width (∘) carrying 1526.0 A in anti-phase and two rings of 30 cm width (∗) carrying 1841.6 A in anti-phase, both at frequency $f = 1,000$ Hz. (**a**) Amplitude of the current distribution; (**b**) Magnetic field B_z along the z-axis

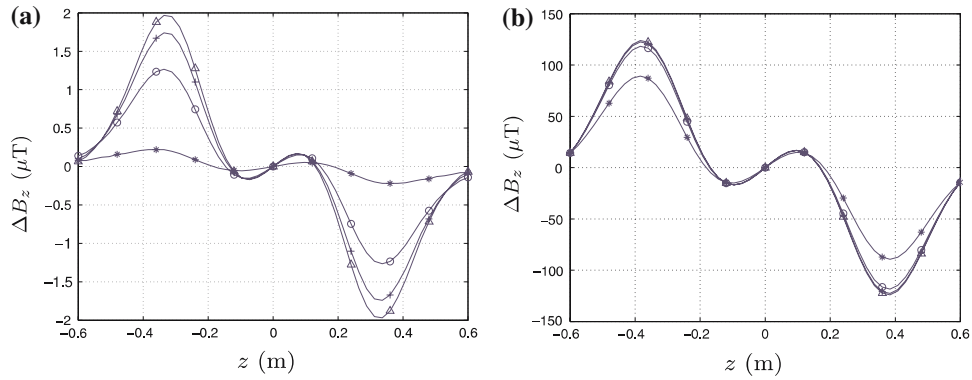

Fig. 7 Difference between the B_z-field at $f = 0$ Hz and $f = 100$ Hz ($*$), $f = 400$ Hz ($\circ$), $f = 700$ Hz ($+$), $f = 1,000$ Hz ($\triangle$). (**a**) Two rings of 4 cm width carrying 1526.0 A in anti-phase; (**b**) Two rings of 30 cm width carrying 1841.6 A in anti-phase

gradient is approximately 3 μT/m, meaning that the relative error is of the order 10^{-4}. For the 30 cm case, the relative error is almost 10 times greater, i.e., of the order 10^{-3}. Thus, the use of wider rings entails greater errors in the gradient of the field.

The increase of the gradient of B_z at the origin is due to the edge-effects, induced by the eddy currents. In MRI, this deviation causes errors in the images. So, a time-varying current in the rings generates not the same field as the DC current the pair has been designed for. This error can be compensated by the current supply. If we know the error of the field as a percentage of the desired field, the applied current should be decreased with the same percentage. Due to linearity of the system, the error in the gradient is then compensated.

In the error analysis, we only consider a small area around $z = 0$. In a larger area, errors increase. We see that we cannot realize a linear magnetic field within a large region of interest with a Maxwell pair; more turns are needed. Further, the use of more turns yields a reduction of the total dissipated power. In the next section we consider a realistic z-coil, modeled by 24 rings on the cylinder.

The resistance and the self-inductance of a set of two rings is determined in the same way as for one ring. Also, the obtained results show a similar behavior. Again, a point of inflection is found at the same characteristic frequency as for one ring (in accordance with (53)).

4.3 A realistic z-coil

The third example we consider is a set of 24 rings, where all 24 rings have a width of 2 cm and a radius of 35 cm. The positions are determined by a gradient coil design program. In this program, the magnetic energy is minimized, subject to the requirements that the gradient of the magnetic field at the origin is 1.0×10^4 μT/m, and the second, third, and fourth-order z-dependence are zero. The design program, [14], determines a pattern of streamlines of the current, on basis of which a set of 24 rings is selected. The resulting begin and end positions of the rings are listed in Table 2. The total current in each ring is 180.52 A, but not all currents are in phase. In Table 2, the phases are given in the column called *Dir.*; 1 stands for a current in phase and -1 for one in anti-phase.

In Fig. 8, the amplitude of the current density is shown for an applied frequency of 1,000 Hz. The average current density in each ring is equal to

$$j^c = \frac{1}{D} \sum_{l=1}^{L} I_l = 9.03 \times 10^3 \text{ A/m}. \tag{55}$$

Table 2 Positions of rings and directions of currents in realistic z-coil

Ring	Left	Right	Dir.	Ring	Left	Right	Dir.
1	−0.5277	−0.5077	−1	13	0.0306	0.0506	−1
2	−0.4267	−0.4067	−1	14	0.0738	0.0938	−1
3	−0.3753	−0.3553	−1	15	0.1572	0.1772	1
4	−0.3386	−0.3186	−1	16	0.1896	0.2096	1
5	−0.3090	−0.2890	−1	17	0.2151	0.2351	1
6	−0.2830	−0.2630	−1	18	0.2389	0.2589	1
7	−0.2589	−0.2389	−1	19	0.2630	0.2830	1
8	−0.2351	−0.2151	−1	20	0.2890	0.3090	1
9	−0.2096	−0.1896	−1	21	0.3186	0.3386	1
10	−0.1772	−0.1572	−1	22	0.3553	0.3753	1
11	−0.0938	−0.0738	1	23	0.4067	0.4267	1
12	−0.0506	−0.0306	1	24	0.5077	0.5277	1

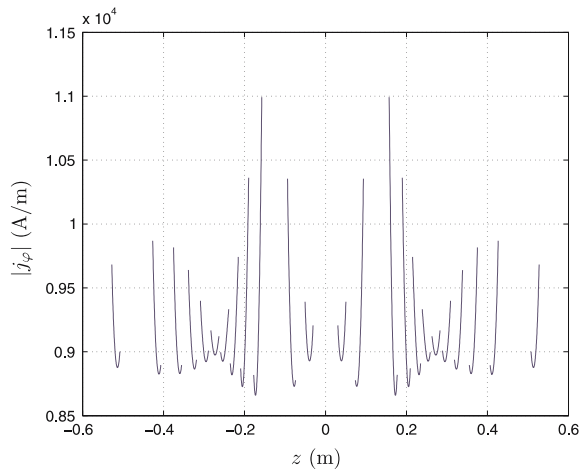

Fig. 8 Amplitude of the current distribution in a set of 24 rings representing a z-coil. Each ring carries a current of 180.52 A at frequency $f = 1,000$ Hz

We observe local edge-effects in the rings as well as a global edge-effect in the whole system. We see how opposite currents amplify each other (e.g. in the two halves of the coil), whereas currents in the same direction damp each other (e.g. within one half of the coil). More or less similar patterns are found by Carlson in [26, Fig. 4], Crozier et al. [27, Figs. 6, 8], and Forbes et al. [28, Figs. 3, 5, 7] all for RF-coils consisting of sets of parallel plane strips in axial direction on a cylinder.

In Fig. 9, the magnetic field of the set of 24 rings is presented. The contour lines of the B_z-field in the (y, z)-plane are shown in Fig. 9(a). The frequency is $f = 1,000$ Hz. The linearity of the field is characterized by parallel contour lines indicating that in a region around the origin the field is linear. In Fig. 9(b), the difference of the field with the DC field is presented by contour lines; this figure gives an indication of the magnitude of the third-order effects. In Fig. 9(c), the magnetic field on the z-axis is shown, for the frequencies $f = 100, 400, 700, 1,000$ Hz. The gradients of the fields are all approximately 1.0×10^4 μT/m, but there is no visible difference on the scale of the figure. Therefore, we zoom in at the differences between the fields generated by alternating currents and by a direct current in Fig. 9(d). The error, i.e., the deviation from the designed value, in the gradient at $f = 1,000$ Hz is approximately 0.5% of the desired gradient. Compensation of the gradient is possible by increasing the applied current in the rings by 0.5%.

The resistance and self-inductance of a set of 24 rings show similar results as before. A point of inflection is found at the characteristic frequency $f_{\text{char}} = 334.0$ Hz, which value is in agreement with (53) for a width of 2 cm.

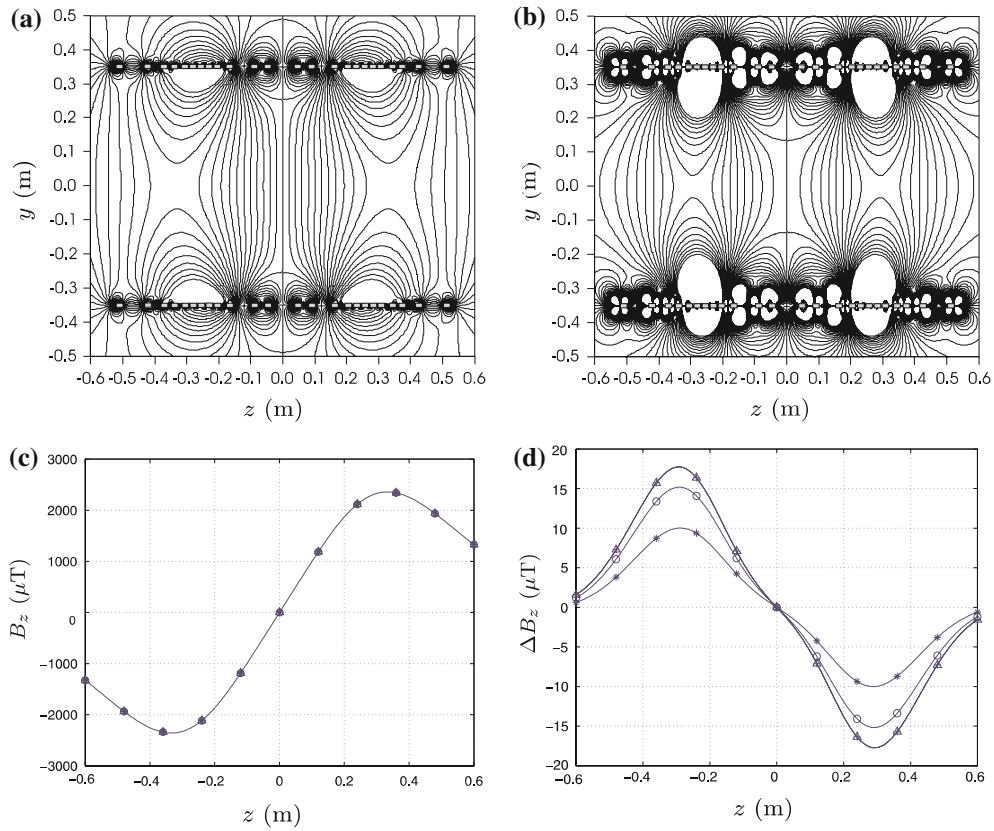

Fig. 9 Magnetic field of a set of 24 rings representing a z-coil. **(a)** Contour lines f B_z at $f = 1,000$ Hz; **(b)** Contour lines of the difference between B_z at $f = 1,000$ Hz and B_z at $f = 0$ Hz; **(c)** B_z on z-axis at $f = 1,000$ Hz; **(d)** Difference between B_z at $f = 100$ Hz $(*)$, $f = 400$ Hz $(\circ)$, $f = 700$ Hz $(+)$, $f = 1,000$ Hz $(\triangle)$ and B_z at $f = 0$ Hz on z-axis

To conclude we show that the total dissipated power in a set of 24 rings is less than that in a set of 2 rings. For the Maxwell pair of two rings of 4 cm width, at a frequency of 1,000 Hz, $\bar{R}$ and $\bar{L}$ are calculated as

$$\bar{R} = 9.6 \times 10^{-4}\,\Omega, \qquad \bar{L} = 3.09 \times 10^{-6}\,\mathrm{H}. \tag{56}$$

For a current $I = 1526.0$ A, the time-averaged magnetic energy is determined from (47):

$$\bar{U}_m = \frac{1}{2}\bar{L}I^2 = 3.60\,\mathrm{J}, \tag{57}$$

while the dissipated power follows from (45) as

$$\bar{P}_{\mathrm{diss}} = I^2\bar{R} = 2.24 \times 10^3\,\mathrm{W}. \tag{58}$$

For the set of 24 rings, at $f = 1,000$ Hz, we calculated

$$\bar{R} = 2.6 \times 10^{-2}\,\Omega, \qquad \bar{L} = 1.32 \times 10^{-4}\,\mathrm{H}. \tag{59}$$

From this, we obtain for currents equal to $I = 180.52$ A,

$$\bar{U}_m = 2.15\,\mathrm{J}, \qquad \bar{P}_{\mathrm{diss}} = 0.847 \times 10^3\,\mathrm{W}. \tag{60}$$

Hence, the total dissipated power in a set of 24 rings is less than that in a set of 2 rings, while in both situations the same gradient in the magnetic field is created. The overall advantage is that the current that has to be supplied to the 24 rings is almost ten times less than the one needed in the set of 2 rings to create the same gradient.

5 Conclusions

The z-coil, a specific gradient coil in an MRI-scanner, is modeled as a set of parallel rings on a cylinder and the current in the thin rings is modeled as a surface current. This model yields an integral equation of the second kind for the current density. An adapted Galerkin method with global basis functions is the dedicated method for the considered configurations. Legendre polynomials are an appropriate choice to describe the dependence of the current with respect to the transverse direction. The use of explicit formulae for the special functions makes our implementation very efficient from a computational point of view. We have made numerical simulations for different sets of one and two or more rings yielding the current distributions in the rings and the induced magnetic fields. Moreover, we calculated aspects such as resistance, self-inductance and dissipated power.

The kernel of the integral equation for the current density contains a singular logarithmic part; this part describes the principal behavior of the currents. The contribution of the regular part of the kernel is small, in the order of one percent of the total current. For designers, neglecting this part is an acceptable option. The kernel of the integral equation for a set of plane rectangular strips is purely logarithmic. From this, we conclude that the characteristic effects for ring-shaped configurations are well described, certainly qualitatively but in an acceptable degree of accuracy also quantitatively, by a corresponding set of plane rectangular strips. This is one of the main conclusions of this research, and very relevant to speed up the simulations needed in the design and development of gradient coils.

Our results show how the induced eddy currents in the rings lead to edge-effects, which increase for increasing frequencies. This edge-effect is more pronounced for wider rings. Sets of many rings show besides a local edge-effect (for one ring) also a global edge-effect (for the set as a whole).

From the simulations for the resistance and the self-inductance we conclude that there exists a characteristic frequency f_{char} at which prevailing resistive effects with respect to inductive effects change into prevailing inductive effects. This f_{char} is inversely proportional to the width of the ring. The resistance of a gradient coil increases with the frequency, whereas the self-inductance decreases with the frequency.

We have shown that for the design of a gradient coil that delivers a gradient which is uniform over a longer distance, a coil of many, much more than two, coils is needed. In preparing such a more realistic coil of 24 rings using a design based on a uniform distributed current over the rings (the DC-distribution), we saw that this yields a small deviation of the actual (dynamic) gradient from the designed (static) one. This deviation can be corrected by a small adjustment of the amplitude of the driving current. Moreover, we found that such a coil has a much lower power dissipation and needs less current to create the same gradient than, for instance, a coil of two rings.

For all simulations performed for the examples given in this paper, the computation times were in the order of one second (on a PC with an Intel Pentium 3 processor at 797 MHz, and 256 MB of RAM). However, if one wants to simulate large gradient coils of many rings, we recommend the following modifications.

First, the Galerkin matrix $\mathbf{A}$ is dense, but diagonally dominant. We may replace $\mathbf{A}$ by $\mathbf{A}_\tau$, where $\mathbf{A}_\tau$ is obtained by dropping all elements whose values are less than τ, i.e., $|A_{ij}| < \tau$ (τ is often called a drop tolerance), thus eliminating much of the set up time. The reason that the off-diagonal elements become smaller when they are further removed from the diagonal is that the distance between the two respective strips increases, resulting in smaller mutual inductions.

Second, the kernel function in the integral equation is logarithmically singular. Using only the logarithmic part, we obtain the principal part of the solution. The resulting integration can be done analytically, leading to a simple formula. The elements of $\mathbf{A}$ emanating from this principal part are all on the diagonal of $\mathbf{A}$; this explains why the matrix $\mathbf{A}$ is very diagonally dominant. The remaining parts are regular and have been computed numerically, but their contributions to $\mathbf{A}$ are much smaller than those of the principal part. These computations concern numerical integrations that become time consuming if the order of the basis functions is high. These regular parts have been computed to get an exact solution. However, if we neglect

them, then the errors will be within one percent of the total solution. Moreover, the computation time will be reduced by more than 90%.

References

1. Chen CN, Hoult DI (1989) Biomedical magnetic resonance technology. Hilger, Bristol
2. Vlaardingerbroek MT, den Boer JA (1999) Magnetic resonance imaging. Springer-Verlag, Berlin
3. Ulicevic T, Kroot JMB, van Eijndhoven SJL, van de Ven AAF (2005) Current distribution in a parallel set of conducting strips. J Eng Math 51:381–400
4. Atkinson KE (1976) A survey of numerical methods for the solution of Fredholm integral equations of the second kind. Philadelphia Society for Industrial and Applied Mathematics
5. Atkinson KE (1997) The numerical solution of integral equations of the second type. Cambridge University Press, Cambridge
6. Romeo F, Hoult DI (1984) Magnetic field profiling: analysis and correcting coil design. Magn Reson Med 1:44–65
7. Suits H, Wilken DE (1989) Improving magnetic field gradient coils for nmr imaging. J Phys E: Instrument 22:565–573
8. Wong E, Jesmanowicz A (1991) Coil optimization for mri by conjugate gradient descent. Magn Reson Med 21:39–48
9. Crozier S, Doddrell DM (1993) Gradient coil design by simulated annealing. J Magn Reson 103:354–357
10. Frenkiel TA, Jasinski A, Morris PG (1988) Apparatus for generation of magnetic field gradient wave forms. J Phys E: Sci Instrument 21:374–377
11. Siebold H (1990) Gradient field coils for mr imaging with high spectral purity. IEEE Trans Magn 26:897–900
12. Turner R (1986) A target field approach for optimal coil design. J Phys D: Appl Phys 19:147–151
13. Peeren GN (2003) Stream function approach for determining optimal surface currents. PhD thesis, Eindhoven University of Technology
14. Peeren GN (2003) Stream function approach for determining optimal surface currents. J Comp Phys 191:305–321
15. Tomasi D (2001) Stream function optimization for gradient coil design. Magn Reson Med 45:505–512
16. Kovetz A (1990) The principles of electromagnetic theory. Cambridge University Press, Cambridge
17. Stratton JA (1941) Electromagnetic theory. McGraw-Hill, London
18. Klinkenbusch L (1996) Theorie der sphärischen Absorberkammer und des mehrschaligen Kugelschirmes. Habilitationsschrift Ruhr-Universität Bochum, Bochum
19. Vossen SHJA (2003) A two-wire antenna system for detecting objects in a homogeneous dielectric half space. PhD thesis, Eindhoven University of Technology
20. Abramowitz M, Stegun IA (1968) Handbook of mathematical functions with formulas graphs and mathematical tables Dover Publications, New York
21. Gradshteyn IS, Ryzhik IM (1994) Table of integrals series and products. Academic Press, New York
22. Kroot JMB (2005) Analysis of eddy currents in a gradient coil. PhD thesis, Eindhoven University of Technology
23. Smythe WR (1968) Static and dynamic electricity. Mc Graw-Hill, New York
24. Reade JB (1979) Asymptotic behavior of eigen-values of certain integral equations. Proc Edinburgh Math Soc 22:137–144
25. Jin JM (1999) Electromagnetic analysis and design in magnetic resonance imaging. CRC Press, London
26. Carlson JW (1986) Currents and fields of thin conductors in rf saddle coils. Magn Reson Med 3:778–790
27. Crozier S, Forbes LK, Roffmann WU, Luescher K, Doddrell DM (1997) A Methodology for current density calculations in high-frequency RF resonators. Concepts Magn Reson 9:195–210
28. Forbes LK, Crozier S, Doddrell DM (1997) Calculating current densities and fields produced by shielded magnetic resonance imaging probes. SIAM J Appl Math 57:401–425